Interplay between relativistic energy corrections and resonant excitations in x-ray multiphoton ionization dynamics of Xe atoms

Koudai Toyota (豊田広大),[1,*] Sang-Kil Son (손상길),[1,†] and Robin Santra[1,2,‡]

[1]*Center for Free-Electron Laser Science, DESY, 22607 Hamburg, Germany*
[2]*Department of Physics, University of Hamburg, 20355 Hamburg, Germany*

In this paper, we theoretically study x-ray multiphoton ionization dynamics of heavy atoms taking into account relativistic and resonance effects. When an atom is exposed to an intense x-ray pulse generated by an x-ray free-electron laser (XFEL), it is ionized to a highly charged ion via a sequence of single-photon ionization and accompanying relaxation processes, and its final charge state is limited by the last ionic state that can be ionized by a single-photon ionization. If x-ray multiphoton ionization involves deep inner-shell electrons in heavy atoms, energy shifts by relativistic effects play an important role in ionization dynamics, as pointed out in Phys. Rev. Lett. **110**, 173005 (2013). On the other hand, if the x-ray beam has a broad energy bandwidth, the high-intensity x-ray pulse can drive resonant photoexcitations for a broad range of ionic states and ionize even beyond the direct one-photon ionization limit, as first proposed in Nat. Photon. **6**, 858 (2012). To investigate both relativistic and resonance effects, we extend the XATOM toolkit to incorporate relativistic energy corrections and resonant excitations in x-ray multiphoton ionization dynamics calculations. Charge-state distributions are calculated for Xe atoms interacting with intense XFEL pulses at a photon energy of 1.5 keV and 5.5 keV, respectively. For both photon energies, we demonstrate that the role of resonant excitations in ionization dynamics is altered due to significant shifts of orbital energy levels by relativistic effects. Therefore, it is necessary to take into account both effects to accurately simulate multiphoton multiple ionization dynamics at high x-ray intensity.

I. INTRODUCTION

The interaction between x-ray photon and matter is characterized by photoionization and accompanying relaxation processes. X-ray photoionization predominantly creates a hole in an inner shell of atoms, which subsequently relaxes via Auger decay or fluorescence. A series of decay processes, a so-called decay cascade, can occur if the hole is formed in a deep inner shell [1–5]. The interaction with x rays becomes rather complex when the sample is exposed to the unprecedentedly high fluence generated by x-ray free-electron lasers (XFELs) [6–9]. Beyond the one-photon saturation fluence, which is the inverse of the single-photon ionization cross section [10], a single atom can absorb more than one photon sequentially after or during decay cascades, and then it becomes a highly charged ion. In this sequential multiphoton ionization model, the final charge is determined by the last ionic state that can be ionized by one-photon ionization. This is called "direct one-photon ionization limit."

The straightforward sequential multiphoton ionization model has been solved with a rate-equation approach [11,12] and verified with a series of XFEL experiments on gas-phased atoms: light atoms such as Ne [11,13] and Ar [14], and heavy atoms such as Kr [15] and Xe [14,16,17]. For example, the calculated charge-state distribution (CSD) of Xe at 2 keV showed an excellent agreement with experimental data [16]. For Xe at 1.5 keV, however, the highest charge of the experimental CSD exceeded by far the theoretical prediction of the direct one-photon ionization limit [16]. To explain this

discrepancy, it has been proposed that multiple resonant excitations followed by Auger-like decays, combined with the broad energy bandwidth of SASE XFEL pulses [6], can drive further ionization beyond the direct one-photon ionization limit. This is called resonance-enabled or resonance-enhanced x-ray multiple ionization (REXMI) [15,16] and this mechanism has been implemented in Refs. [18,19]. Also the importance of single resonant excitation was found in the study of the Ne atom experimentally [11] and theoretically [20].

When an x-ray photon with higher energy interacts with a heavy atom such as xenon, a deeper inner-shell electron is ionized. It induces not only more complicated ionization dynamics, but also it is expected that deep inner-shell energy levels are shifted and split due to relativistic effects. A recent study of Xe at 5.5 keV hinted at this, showing fairly good agreement between theory and experiment, but the theoretical prediction underestimated the yields of highly charged ions due to lack of relativistic effects [17].

Here we present how relativistic energy corrections and resonant excitations influence x-ray multiphoton ionization dynamics. For this purpose, we extend the XATOM toolkit [21–23]. Our implementation allows us to turn on and off the relativistic effect and the resonance effect, separately. This allows us to explore the interplay between both classes of effects on x-ray multiphoton ionization dynamics.

This paper is organized as follows. In Sec. II, we introduce our basic equations and notations, and then we formulate relativistic energy corrections, cross sections, and rates. We also discuss how to simulate x-ray multiphoton ionization dynamics by using a Monte Carlo approach [24], emphasizing the numerical challenge to handle an extremely large configurational space when resonant excitations are included. In Sec. III, we present calculations of CSDs for Xe at 1.5 keV and 5.5 keV, which correspond to XFEL experiments conducted

*koudai.toyota@cfel.de
†sangkil.son@cfel.de
‡robin.santra@cfel.de

at LCLS [16] and SACLA [17], respectively, and discuss both relativistic and resonance effects on x-ray multiphoton ionization dynamics. In Sec. IV, we conclude and give future perspectives.

II. THEORY AND NUMERICAL DETAILS

In this section, we start with the nonrelativistic Hartree-Fock-Slater (HFS) equation and provide relativistic energy corrections to the orbital energy levels. These are used to calculate photoionization cross sections, Auger rates, fluorescence rates, and resonant photoexcitation cross sections including relativistic effects. This relativistic framework is implemented as an extension of the XATOM toolkit [21–23]. The basic framework can be found in Ref. [25]. All formulas below can be derived with standard angular-momentum algebra [26]. At the end of this section, we will discuss numerical challenges to simulate x-ray multiphoton ionization dynamics when taking into consideration relativistic and resonance effects.

A. Nonrelativistic Hartree-Fock-Slater equation

We start from a nonrelativistic treatment based on the Hartree-Fock-Slater (HFS) method. The effective one-electron Schrödinger equation for an atom is

$$\left[-\tfrac{1}{2}\nabla^2 + V(\mathbf{r})\right]\psi(\mathbf{r}) = \varepsilon\psi(\mathbf{r}). \tag{1}$$

Atomic units are used unless specified otherwise. The potential $V(\mathbf{r})$ is written as

$$V(\mathbf{r}) = -\frac{Z}{r} + \int d^3r' \frac{\rho(\mathbf{r}')}{|\mathbf{r}-\mathbf{r}'|} + V_{\mathrm{x}}(\mathbf{r}), \tag{2}$$

where Z is the nuclear charge of the atom, and the exchange potential $V_{\mathrm{x}}(\mathbf{r})$ is approximated by the Slater exchange potential [27],

$$V_{\mathrm{x}}(\mathbf{r}) = -\frac{3}{2}\left[\frac{3}{\pi}\rho(\mathbf{r})\right]^{1/3}. \tag{3}$$

The electronic density $\rho(\mathbf{r})$ is given by

$$\rho(\mathbf{r}) = \sum_i^{N_{\mathrm{elec}}} \psi_i^\dagger(\mathbf{r})\psi_i(\mathbf{r}), \tag{4}$$

where $\psi_i(\mathbf{r})$ represents the spin orbital of the ith electron, and the summation runs over the number of electrons N_{elec}. We employ a spherically symmetric electronic density, i.e., $\rho(\mathbf{r}) \to \rho(r)$, then the potential becomes also spherically symmetric: $V(\mathbf{r}) \to V(r)$. In addition, we use the Latter tail correction [28] to obtain the proper long-range potential for both occupied and unoccupied orbitals. Hence the spherically symmetric potential is given by

$$V(r) = \begin{cases} -\frac{Z}{r} + \int d^3r' \frac{\rho(r')}{|\mathbf{r}-\mathbf{r}'|} - \frac{3}{2}\left[\frac{3}{\pi}\rho(r)\right]^{1/3} & \text{for } r < r_c, \\ -\frac{Z-N_{\mathrm{elec}}+1}{r} & \text{for } r \geqslant r_c, \end{cases} \tag{5}$$

where r_c is determined such that $V(r)$ is continuous at $r = r_c$.

Let us consider a spin-orbital $\psi_i(\mathbf{r})$ given in nlm_lm_s representation, where n, l, m_l, and m_s are the principal quantum number, the orbital angular momentum quantum number, the associated projection quantum number, and the

spin magnetic quantum number, respectively. It is then written as

$$\psi_{nlm_lm_s}(\mathbf{r}) = \frac{u_{nl}(r)}{r}Y_{lm_l}(\Omega)\chi_{m_s}, \tag{6}$$

where $Y_{lm_l}(\Omega)$ is a spherical harmonic and χ_{m_s} is a Pauli two-component spinor. The function $u_{nl}(r)$ satisfies the radial part of the HFS equation of Eq. (1),

$$\left[-\frac{1}{2}\frac{d^2}{dr^2} + \frac{l(l+1)}{2r^2} + V(r)\right]u_{nl}(r) = \varepsilon_{nl}u_{nl}(r). \tag{7}$$

To solve the HFS eigenvalue problem of Eq. (7), we employ the generalized pseudospectral (GPS) method based on the Legendre polynomials [29]. Let r_{max} be the maximum radius in the numerical calculation. The spatial coordinate $r \in [0, r_{\mathrm{max}}]$ is then mapped onto the finite range $x \in [-1,1]$ by the following relation:

$$r = L\frac{1+x}{1-x+2L/r_{\mathrm{max}}}, \tag{8}$$

where L is a mapping parameter to tune the distribution of the grid points. A small value of L gives us dense grid points near the origin, and a large value of L gives a more uniform distribution of grid points in the interval $[0, r_{\mathrm{max}}]$. The solutions are required to satisfy the boundary conditions $u_{nl}(0) = u_{nl}(r_{\mathrm{max}}) = 0$. The wave functions of initially occupied orbitals are localized near the origin. On the other hand, multiple resonant excitations can excite several electrons to high-n Rydberg states that tend to have large amplitudes away from the origin. An optimal L needs to be chosen to accurately describe both of them.

B. Relativistic energy corrections

We treat relativistic effects within first-order degenerate perturbation theory [30]. The effective one-body relativistic Hamiltonian for two-component spinors is given by [31]

$$\hat{H} = \hat{H}_0 + \hat{H}_{\mathrm{mass}} + \hat{H}_{\mathrm{dar}} + \hat{H}_{\mathrm{so}}, \tag{9}$$

where $\hat{H}_0$ is the nonrelativistic Hamiltonian given in Eq. (1) as the unperturbed term,

$$\hat{H}_0 = -\tfrac{1}{2}\nabla^2 + V(r). \tag{10}$$

The rest ($\hat{H}' = \hat{H}_{\mathrm{mass}} + \hat{H}_{\mathrm{dar}} + \hat{H}_{\mathrm{so}}$) are the leading-order relativistic corrections, which we treat as perturbations. The relativistic energy corrections are calculated with these perturbative terms and the nonrelativistic spin orbitals of Eq. (6).

The first is the mass term,

$$\hat{H}_{\mathrm{mass}} = -\frac{\alpha^2}{8}\hat{p}^4, \tag{11a}$$

where $\hat{p}$ is the canonical momentum operator and α is the fine-structure constant ($\alpha = 1/c$, where c is the speed of light). The mass term represents the relativistic mass correction for an electron orbiting at a speed close to c. The second is the Darwin term,

$$\hat{H}_{\mathrm{dar}} = -\frac{\alpha^2}{4}\frac{dV}{dr}\frac{d}{dr}, \tag{11b}$$

TABLE I. Comparison of orbital energy levels of neutral Xe atom (in eV). "Nonrel" refers to nonrelativistic calculations obtained from Eq. (7), and "Rel" means relativistic calculations using Eq. (15). DFS indicates the Dirac-Fock-Slater results taken from Ref. [33] and Expt. is the experimental data taken from Ref. [35].

Orbital	Nonrel	E_{mass}	E_{dar}	E_{so}	Rel	DFS [33]	Expt. [35]
$1s_{1/2}$	−33102.77	−7070.30	5565.00	0	−34608.06	−34555.26	−34561
$2s_{1/2}$	−5057.17	−972.53	587.98	0	−5441.71	−5417.15	−5453
$2p_{1/2}$	−4771.10	−168.53	−2.46	−199.98	−5141.09	−5104.13	−5107
$2p_{3/2}$				99.49	−4842.60	−4774.49	−4786
$3s_{1/2}$	−1045.69	−205.99	117.54	0	−1134.15	−1122.22	−1148.7
$3p_{1/2}$	−922.75	−42.87	−0.46	−37.84	−1003.94	−989.73	−1002.1
$3p_{3/2}$				18.92	−947.18	−926.51	−940.6
$3d_{3/2}$	−692.12	−11.21	−0.28	−8.08	−711.71	−690.88	−689.0
$3d_{5/2}$				5.39	−698.24	−677.35	−676.4
$4s_{1/2}$	−192.78	−46.02	25.82	0	−212.99	−208.50	−213.2
$4p_{1/2}$	−148.44	−9.32	−0.09	−7.65	−165.52	−160.81	−146.7
$4p_{3/2}$				3.82	−154.03	−148.00	−145.5
$4d_{3/2}$	−71.42	−2.17	−0.04	−1.28	−74.93	−69.85	−69.5
$4d_{5/2}$				0.85	−72.79	−67.77	−67.5
$5s_{1/2}$	−21.78	−6.84	3.82	0	−24.80	−23.65	−23.3
$5p_{1/2}$	−11.39	−1.05	−0.01	−0.84	−13.30	−12.39	−13.4
$5p_{3/2}$				0.42	−12.03	−10.97	−12.1

which may be interpreted in terms of Zitterbewegung [32]. The last is the spin-orbit coupling term,

$$\hat{H}_{so} = \frac{\alpha^2}{2}\frac{1}{r}\frac{dV}{dr}\hat{l}\cdot\hat{s}. \qquad (11c)$$

Let the operator $\hat{j}$ be the sum of the orbital angular momentum operator $\hat{l}$ and the spin angular momentum operator $\hat{s}$, then $\hat{j} = \hat{l} + \hat{s}$. In the following, we introduce the $nljm$ representation of a spin orbital,

$$\phi_{nljm}(\mathbf{r}) = \sum_{m_l m_s} C(lsj; m_l m_s m)\psi_{nlm_l m_s}(\mathbf{r}), \qquad (12)$$

to calculate relativistic energy corrections and rates. Here the symbol $C(lsj; m_l m_s m)$ represents a Clebsch-Gordan coefficient ($s = \frac{1}{2}$). The spin orbital $\phi_{nljm}(\mathbf{r})$ is a simultaneous eigenfunction of $\hat{l}^2$, $\hat{s}^2$, $\hat{j}^2$, and $\hat{j}_z$. Let $\hat{O}$ be an operator that is independent of angular degrees of freedom. Then,

$$\int d^3r\, \phi^\dagger_{nljm}(\mathbf{r})\hat{O}\phi_{nlj'm'}(\mathbf{r}) = \langle\hat{O}\rangle_{nl}\delta_{jj'}\delta_{mm'}, \qquad (13a)$$

where

$$\langle\hat{O}\rangle_{nl} = \int_0^\infty dr\, r^2\left(\frac{u^*_{nl}(r)}{r}\right)\hat{O}\left(\frac{u_{nl}(r)}{r}\right), \qquad (13b)$$

and $u_{nl}(r)$ is an eigenfunction of Eq. (7). We evaluate the matrix elements of Eqs. (11) in the $nljm$ representation of Eq. (12) with the use of Eq. (7). Then, the relativistic energy shifts are given by

$$\Delta\varepsilon^{mass}_{nl} = \frac{\alpha^2}{2}\langle(\varepsilon_{nl} - V(r))^2\rangle_{nl}, \qquad (14a)$$

$$\Delta\varepsilon^{dar}_{nl} = -\frac{\alpha^2}{4}\left\langle\frac{dV}{dr}\frac{d}{dr}\right\rangle_{nl}, \qquad (14b)$$

$$\Delta\varepsilon^{so}_{nlj} = \begin{cases} 0 & \text{for } j = \frac{1}{2}, \\ \frac{\alpha^2}{4}l\langle\frac{1}{r}\frac{dV}{dr}\rangle_{nl} & \text{for } j = l + \frac{1}{2}, \\ -\frac{\alpha^2}{4}(l+1)\langle\frac{1}{r}\frac{dV}{dr}\rangle_{nl} & \text{for } j = l - \frac{1}{2}. \end{cases} \quad (14c)$$

Therefore, an orbital energy level including relativistic energy corrections in the $nljm$ representation is given by

$$E_{nlj} = \varepsilon_{nl} + \Delta\varepsilon^{mass}_{nl} + \Delta\varepsilon^{dar}_{nl} + \Delta\varepsilon^{so}_{nlj}. \qquad (15)$$

Table I compares the orbital energy levels of neutral Xe including relativistic energy corrections calculated using Eq. (15) with those obtained by Lu *et al.* solving the Dirac-Fock-Slater (DFS) equation [33]. Our results shown in the table were obtained using $N = 150$, $r_{max} = 50$ a.u., and $L = 10$, where N is the number of grid points used in the GPS method. With this parameter set, our calculated values of the mass term in Eq. (11a) and the Darwin term in Eq. (11b) for the $1s_{1/2}$ orbital deviate 6.3% and 8.0% from those (not shown) in Ref. [30], respectively. Substituting these values into Eq. (15), the relativistic $1s_{1/2}$ orbital energy agrees with that in Refs. [30,33,34] to within 0.2%. Overall, our calculated orbital energies agree with the reference values to within better than 10%. The same set of numerical parameters is used in the following subsections for calculating cross sections and rates.

C. Photoionization cross section

The photoionization cross section of a subshell i at incident photon energy ω_{in} is given by

$$\sigma_p(i,\omega_{in}) = \frac{4}{3}\pi^2\alpha\omega_{in}N_i\sum_{l_a=|l_i\pm1|}\frac{l_>}{2l_i+1}\left|\langle u_{E_a l_a}|r|u_{n_i l_i}\rangle\right|^2, \qquad (16)$$

where N_i is the number of electrons in the subshell i, and $l_>$ is the greater of l_i and l_a. The energy $E_a(>0)$ of a final state a is given by $E_a = E_{n_i l_i j_i} + \omega$, where the quantity $E_{n_i l_i j_i}$ is an

TABLE II. Comparison of photoionization cross sections of neutral Xe atom at 5455 keV (in kbarns). "Nonrel" refers to nonrelativistic calculations using Eq. (6) in Ref. [22], and "Rel" is relativistic calculations using Eq. (16). DFS results are taken from Ref. [38].

Orbital	Nonrel	Rel	DFS [38]
$2s_{1/2}$	23.96	28.05	23.37
$2p_{1/2}$	110.56	47.69	40.96
$2p_{3/2}$		77.39	73.73
$3s_{1/2}$	5.49	5.76	5.54
$3p_{1/2}$	15.14	5.31	5.75
$3p_{3/2}$		10.25	10.34
$3d_{3/2}$	8.28	3.36	3.56
$3d_{5/2}$		4.99	4.95
$4s_{1/2}$	1.24	1.25	1.26
$4p_{1/2}$	2.96	0.99	1.13
$4p_{3/2}$		1.98	2.02
$4d_{3/2}$	1.34	0.54	0.57
$4d_{5/2}$		0.80	0.79
$5s_{1/2}$	0.18	0.18	0.19
$5p_{1/2}$	0.32	0.10	0.12
$5p_{3/2}$		0.21	0.21

orbital energy level including relativistic energy corrections, Eq. (15). Here, $u_{E_a l_a}$ is the continuum state with the positive energy E_a, which is computed using the fourth-order Runge-Kutta method on a uniform grid [36,37]. The selection rules are

$$j_a = j_i, j_i \pm 1, \tag{17a}$$

$$l_a = l_i \pm 1. \tag{17b}$$

Table II compares our results with the values calculated by using DFS [38]. The deviations between them are found to be larger for deep inner shells. Since relativistic energy corrections lower orbital energy levels, relativistic photoionization cross sections summed over different j's become bigger than those in the nonrelativistic case. Note that Table II shows photoionization cross sections of the ground configuration of neutral Xe atom only. For most multiple-hole states arising as a consequence of strong x-ray exposure, as discussed in Sec. II G, one cannot simply consult the literature.

D. Auger rate

The Auger rate at which an initial hole in a subshell i is refilled by an electron from a subshell q or q' accompanied by the emission of an Auger electron from the subshell q or q' is given by [39]

$$\Gamma_{i,qq'} = 2\pi N_i^{\mathrm{H}} N_{qq'} \sum_{l_a=0}^{l_i+l_q+l_{q'}} \sum_{j_a=|l_a-\frac{1}{2}|}^{l_a+\frac{1}{2}} \sum_{J=|j_q-j_{q'}|}^{j_q+j_{q'}} (2j_a+1)$$
$$\times (2J+1)|M_J(aiqq')|^2. \tag{18}$$

The kinetic energy of the Auger electron is given by $E_a = -E_{n_i l_i j_i} + E_{n_q l_q j_q} + E_{n_{q'} l_{q'} j_{q'}}$. The constant N_i^{H} is the number of initial holes in the subshell i. Let N_q be the number of electrons in the subshell q; then the quantity $N_{qq'}$ is defined

by

$$N_{qq'} = \begin{cases} N_q N_{q'} & \text{(inequivalent electrons)}, \\ \frac{2j_q+1}{2j_q} N_q(N_q-1) & \text{(equivalent electrons)}. \end{cases} \tag{19}$$

The function $M_J(aiqq')$ is defined by

$$M_J(aiqq') = \tau \sum_{k=0}^{l_i+l_q+l_{q'}} [R_k(aiqq')A_{kJ}(aiqq')$$
$$+ (-1)^{-J} R_k(aiq'q)A_{kJ}(aiq'q)], \tag{20a}$$

where the coefficient τ is given by

$$\tau = \begin{cases} 1 & \text{(inequivalent electrons)}, \\ \frac{1}{\sqrt{2}} & \text{(equivalent electrons)}. \end{cases} \tag{20b}$$

The function $R_k(aiqq')$ is defined by

$$R_k(aiqq') = \int_0^\infty dr \int_0^\infty dr' \, u_{E_a l_a}(r) u_{n_i l_i}(r')$$
$$\times \frac{r_<^k}{r_>^{k+1}} u_{n_q l_q}(r) u_{n_{q'} l_{q'}}(r'), \tag{20c}$$

where $r_>(r_<)$ is the greater (lesser) of r and r', and the function $A_{kJ}(aiqq')$ is defined by

$$A_{kJ}(aiqq') = \begin{Bmatrix} j_a & j_q & k \\ j_{q'} & j_i & J \end{Bmatrix} \begin{Bmatrix} l_q & s & j_q \\ j_a & k & l_a \end{Bmatrix} \begin{Bmatrix} l_{q'} & s & j_{q'} \\ j_i & k & l_i \end{Bmatrix}$$
$$\times \langle l_a ||C_k|| l_q \rangle \langle l_i ||C_k|| l_{q'} \rangle, \tag{20d}$$

where the braces are $6j$ symbols, and

$$\langle l' ||C_k|| l \rangle = \sqrt{2k+1} C(lkl';000). \tag{20e}$$

E. Fluorescence rate

The fluorescence rate at which an initial hole in a subshell q is refilled by an electron from a subshell q' accompanied by the emission of a photon is given by

$$\Gamma_{qq'} = \frac{4}{3}\alpha^3 \left(E_{n_{q'} l_{q'} j_{q'}} - E_{n_q l_q j_q}\right)^3 l_> N_{q'} N_q^{\mathrm{H}} \begin{Bmatrix} l_{q'} & s & j_{q'} \\ j_q & 1 & l_q \end{Bmatrix}^2$$
$$\times \left|\langle u_{n_q l_q} | r | u_{n_{q'} l_{q'}} \rangle\right|^2, \tag{21}$$

where $N_{q'}$ and N_q^{H} represent the number of electrons and holes in the subshells q' and q, respectively. Here it is assumed that the emitted photon is not polarized. The selection rules are

$$j_q = j_{q'}, j_{q'} \pm 1, \tag{22a}$$

$$l_q = l_{q'} \pm 1. \tag{22b}$$

Table III compares our numerical results for Auger (Coster-Kronig) and fluorescence rates with the recent data obtained with the multiconfiguration Dirac-Fock method [40]. It is important to realize that the Coster-Kronig channels of $L_2 - L_3 X$ and $M_2 - M_3 X$ are completely missing in the nonrelativistic case, because they are energetically forbidden without the spin-orbit energy splitting.

TABLE III. Comparison of fluorescence ($L - X$ or $M - X$), Auger ($L - XY$ or $M - XY$), and Coster-Kronig ($L - LX$ or $M - MX$) rates for M- and L-shell vacancies of Xe (in a.u.). "Nonrel" refers to the nonrelativistic calculation and "Rel" is obtained from Eq. (18) or (21). DF refers to the multiconfiguration Dirac-Fock calculations [40]. Note that the Coster-Kronig channels of $L_2 - L_3 X$ and $M_2 - M_3 X$ are energetically forbidden in the nonrelativistic case.

Group	Nonrel	Rel	DF [40]
$L_1 - X$	6.33×10^{-3}	8.03×10^{-3}	6.33×10^{-3}
$L_1 - XY$	6.07×10^{-2}	5.63×10^{-2}	6.50×10^{-2}
$L_1 - L_{23}X$	8.19×10^{-2}	6.76×10^{-2}	5.83×10^{-2}
$L_2 - X$	1.04×10^{-2}	1.32×10^{-2}	5.35×10^{-3}
$L_2 - XY$	9.38×10^{-2}	8.70×10^{-2}	4.86×10^{-2}
$L_2 - L_3 X$	Forbidden	2.01×10^{-2}	6.82×10^{-3}
$L_3 - X$	$(=L_2 - X)$	1.08×10^{-2}	1.01×10^{-2}
$L_3 - XY$	$(=L_2 - XY)$	9.28×10^{-2}	1.10×10^{-1}
$M_1 - X$	1.72×10^{-4}	2.27×10^{-4}	1.72×10^{-4}
$M_1 - XY$	1.85×10^{-2}	1.73×10^{-2}	1.91×10^{-2}
$M_1 - M_{23}X$	4.74×10^{-1}	3.46×10^{-1}	3.72×10^{-1}
$M_1 - M_{45}X$	8.97×10^{-2}	8.06×10^{-2}	8.38×10^{-2}
$M_2 - X$	1.61×10^{-4}	2.19×10^{-4}	1.75×10^{-4}
$M_2 - XY$	2.09×10^{-2}	1.97×10^{-2}	2.10×10^{-2}
$M_2 - M_3 X$	Forbidden	5.39×10^{-3}	6.20×10^{-4}
$M_2 - M_{45}X$	2.05×10^{-1}	1.54×10^{-1}	1.64×10^{-1}
$M_3 - X$	$(=M_2 - X)$	1.75×10^{-4}	1.73×10^{-4}
$M_3 - XY$	$(=M_2 - XY)$	2.06×10^{-2}	2.22×10^{-2}
$M_3 - M_{45}X$	$(=M_2 - M_{45}X)$	1.88×10^{-1}	1.76×10^{-1}
$M_4 - X$	1.02×10^{-5}	1.05×10^{-5}	1.21×10^{-5}
$M_4 - XY$	2.25×10^{-2}	2.23×10^{-2}	2.46×10^{-2}
$M_5 - X$	$(=M_4 - X)$	1.03×10^{-5}	1.05×10^{-5}
$M_5 - XY$	$(=M_4 - XY)$	2.26×10^{-2}	2.16×10^{-2}

F. Resonant photoexcitation cross section

We consider the cross section of a resonant excitation for a bound-to-bound transition from an initial to a final orbital, $i \rightarrow f$,

$$\sigma_R(i \rightarrow f, \omega) = \frac{4}{3}\pi^2 \alpha \omega l_> N_i N_f^H \begin{Bmatrix} l_i & s & j_i \\ j_f & 1 & l_f \end{Bmatrix}^2$$
$$\times \left| \langle u_{n_f l_f} | r | u_{n_i l_i} \rangle \right|^2 \delta(\omega - \Delta E_{fi}), \quad (23a)$$

where the δ function represents the energy conservation law. The quantity ΔE_{fi} represents the transition energy given by

$$\Delta E_{fi} = E_{n_f l_f j_f} - E_{n_i l_i j_i}. \quad (23b)$$

Assuming that the photon energy spectrum is given by a Gaussian function,

$$f(\omega; \omega_{in}) = \frac{1}{\Delta\omega_{in}} \sqrt{\frac{4 \ln 2}{\pi}} e^{-4 \ln 2 (\frac{\omega - \omega_{in}}{\Delta\omega_{in}})^2}, \quad (24)$$

where $\Delta\omega_{in}$ is the full width at half maximum (FWHM) of the photon-energy distribution function. Convolving the cross section with the spectral distribution profile of Eq. (24), we obtain

$$\sigma_R(i \rightarrow f, \omega_{in}) = \frac{4}{3}\pi^2 \alpha \Delta E_{fi} l_> N_i N_f^H \begin{Bmatrix} l_i & s & j_i \\ j_f & 1 & l_f \end{Bmatrix}^2$$
$$\times \left| \langle u_{n_f l_f} | r | u_{n_i l_i} \rangle \right|^2 f(\Delta E_{fi}; \omega_{in}). \quad (25)$$

Replacing the subscript a with f in Eq. (17), we obtain the selection rules.

G. Rate equations for ionization dynamics

We employ a rate-equation approach to simulate x-ray multiphoton ionization dynamics [11,12]. The eigenfunctions and energies of the HFS equation in Eq. (1) are used to calculate the cross sections of Eqs. (16) and (25) and rates of Eqs. (18) and (21). Time-dependent photoionization and photoexcitation rates at a given time are calculated by their respective cross sections times the photon flux at that time. All calculated rates are plugged into a set of coupled rate equations,

$$\frac{dP_I}{dt} = \sum_{I' \neq I}^{\text{allconfig}} [\Gamma_{I' \rightarrow I}(t) P_{I'}(t) - \Gamma_{I \rightarrow I'}(t) P_I(t)], \quad (26)$$

where P_I is the population of the Ith electronic configuration and $\Gamma_{I \rightarrow I'}$ is the transition rate from I to I'.

The dimension of the rate-equation system of Eq. (26) becomes enormously large for heavy atoms. For example, let us consider a neutral Xe atom, which has 54 electrons, and construct all possible electronic configurations that may be formed by removing zero, one, or more electrons, from the neutral ground configuration. All possible configurations of Xe ions, Xe^{q+}, in the nonrelativistic case are written as

$$Xe^{q+}: 1s^{n_1} 2s^{n_2} 2p^{n_3} \ 3s^{n_4} 3p^{n_5} 3d^{n_6} \ 4s^{n_7} 4p^{n_8} 4d^{n_9} \ 5s^{n_{10}} 5p^{n_{11}},$$

where n_i is chosen from zero to the maximum occupation number (n_i^{max}) of the ith subshell, i.e., $n_1 = 0, 1, 2, n_3 = 0, 1, \ldots, 6$, and so on. The sum of $\{n_i\}$ gives the total number of electrons: $\sum_i n_i = 54 - q$. The number of all possible configurations, which is equal to the number of coupled rate equations that must be solved, is given by $N_{config} = \prod_i (n_i^{max} + 1)$. For the Xe case, it gives $3 \times (3 \times 7) \times (3 \times 7 \times 11) \times (3 \times 7 \times 11) \times (3 \times 7) = 70\,596\,603$. When relativistic effects are taken into account, N_{config} is further increased by about 200 times because of the spin-orbit splittings ($p_{1/2}/p_{3/2}$ and $d_{3/2}/d_{5/2}$), so the number of rate equation becomes $15\,069\,796\,875$. If resonant bound-to-bound excitations are considered, N_{config} explodes (see Table I in Ref. [19]), even without consideration of relativistic effects.

Directly solving such a gigantic number of coupled rate equations is thus impractical. Instead, we extend XATOM to employ the Monte Carlo method to solve Eq. (26) with precalculated tables of cross sections and rates, as previously demonstrated in Ref. [24]. Furthermore, the electronic structure, cross sections, and rates are calculated on the fly, only when a Monte Carlo trajectory visits a new electronic configuration [17]. This Monte Carlo on-the-fly scheme dramatically saves computational effort, enabling us to explore very complicated ionization dynamics of heavy atoms. A detailed Monte Carlo description for x-ray multiphoton ionization dynamics is found in Ref. [24]. A Monte Carlo convergence is checked out at every 100 trajectories. When the absolute differences of charge state populations between current and previous checking points become less than 10^{-4} (10^{-5} for the 5.5 keV case in Sec. III A), the program terminates the Monte Carlo calculation.
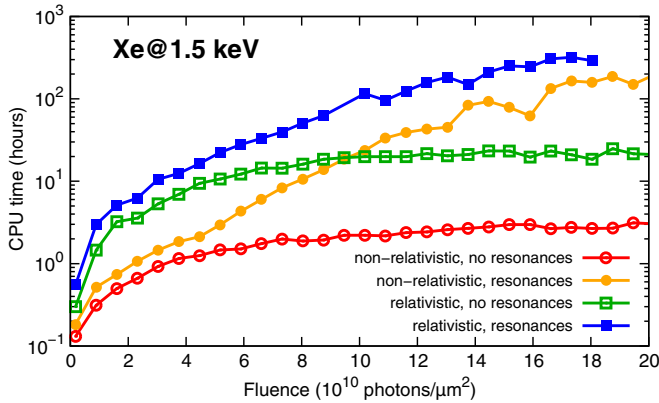
FIG. 1. Comparison of CPU times for calculating x-ray multiphoton ionization dynamics of Xe at 1.5 keV with a bandwidth of 15 eV as a function of fluence. The open circles (red) and open squares (green) represent nonrelativistic and relativistic calculations excluding resonant excitations. The filled circles (orange) and filled squares (blue) represent nonrelativistic and relativistic calculations including resonant excitations.

H. Comparison of computational times

Now we compare computational times for calculating x-ray multiphoton ionization dynamics, turning on and off relativistic and resonance effects. Thus we have four different cases: (a) *nonrel, no res*: without relativistic effects and without resonant excitations; (b) *nonrel, res*: without relativistic effects and with resonant excitations; (c) *rel, no res*: with relativistic effects and without resonant excitations; and (d) *rel, res*: with relativistic effects and with resonant excitations. Figure 1 shows the CPU time for each case as a function of fluence, calculating the charge-state distribution (CSD) of Xe atom at 1.5 keV. A photon energy bandwidth of 15 eV FWHM is used when resonant excitations are included. The pulse duration is fixed at 80 fs FWHM.

First, let us examine the cases excluding resonances, (a) and (c). The relativistic calculations (green, open squares) take longer CPU time by one order of magnitude than the nonrelativistic calculations (red, open circles). In both cases, the computational time saturates as the fluence increases, because the direct one-photon ionization is no longer possible beyond a certain charge state without resonant excitations and all of the Monte Carlo trajectories are stuck at the direct one-photon ionization limit (Xe^{26+} at 1.5 keV). On the other hand, for the cases including resonances, (b) and (d), as plotted with filled circles and filled squares, the CPU time keeps increasing as the fluence increases. This is because resonant excitations open up new ionization channels beyond the direct one-photon ionization limit and Monte Carlo trajectories take more time to arrive at their final charge state as the fluence increases. At the highest fluence ($\sim 2 \times 10^{11}$ photons/μm^2) used in our calculations, the CPU time of the resonant cases is more than one order of magnitude longer than that of the nonresonant cases. Overall, at the highest fluence, the relativistic calculation with resonant excitations takes $\sim$100 times more CPU time than the nonrelativistic calculation without resonant excitations.

TABLE IV. Computational parameters used for ionization dynamics calculations.

	N	L (a.u.)	r_{max} (a.u.)	n_{max}	l_{max}
Xe at 1.5 keV					
Nonrel, no res	150	10	50		
Nonrel, res	150	10	100	21	6
Rel, no res	150	10	50		
Rel, res	150	10	100	19	7
Xe at 5.5 keV					
Nonrel, no res	150	10	50		
Nonrel, res	150	10	100	15	6
Rel, no res	150	10	50		
Rel, res	150	10	100	12	7

It is worthwhile to discuss how to choose computational parameters, especially for calculating the resonant cases. Resonant excitation involves an electronic transition to a Rydberg state. The maximum radius r_{max}, the mapping parameter L, and the number of grid points N must be large enough to provide an accurate description of high-n Rydberg states. Thus they must be varied and checked to obtain converged CSDs. At the same time, it is also necessary to restrict n_{max} and l_{max} when calculating Rydberg states. In principle, the orbital angular momentum quantum number l is given by $0 \leqslant l \leqslant n - 1$, but in practice l_{max} can be chosen much smaller than ($n_{max} - 1$) for two reasons. First, single resonant excitation will increase (or decrease) l by ± 1. Second, REXMI [16] involves multiply excited states and their autoionization, which could potentially give a high-l state. For example, a doubly excited state with two $l = 3$ excited electrons can decay into an $l = 6$ state, and another electronic decay from this state can increase l further. A rule of thumb is to choose l_{max} higher than two times the highest l of the initially occupied subshells. Eventually l_{max} as well as n_{max} should be chosen as convergence parameters. We found that $n_{max} = 21$ and $l_{max} = 6$ are necessary to get converged results for the nonrelativistic resonant case in the fluence regime used in Fig. 1. Note that those are larger than the values ($n_{max} = 10$ and $l_{max} = 4$) used in Refs. [18,19]. In Table IV, we list all computational parameters (N, L, r_{max}, n_{max}, and l_{max}) that we used for the x-ray multiphoton dynamics calculations presented in the following sections.

III. RESULTS

A. X-ray multiphoton ionization dynamics of Xe at 5.5 keV

We investigate x-ray multiphoton ionization dynamics of Xe at 5.5 keV, where theory predicted lower populations for high charge states in comparison with experimental data [17]. It was speculated that this underestimation might be attributed to the lack of relativistic effects and shake-off processes in the theoretical model used. A 5.5 keV photon can ionize L-shell electrons, where the relativistic correction is a few hundred eV and the spin-orbit splitting of $2p$ is about 300 eV (see Table I). Figure 2 shows the L-shell orbital energies of the ground configuration of Xe ions as a function of charge state. The nonrelativistic calculations ($2s$ and $2p$) are plotted with lines and symbols, while the relativistic calculations ($2s_{1/2}$,
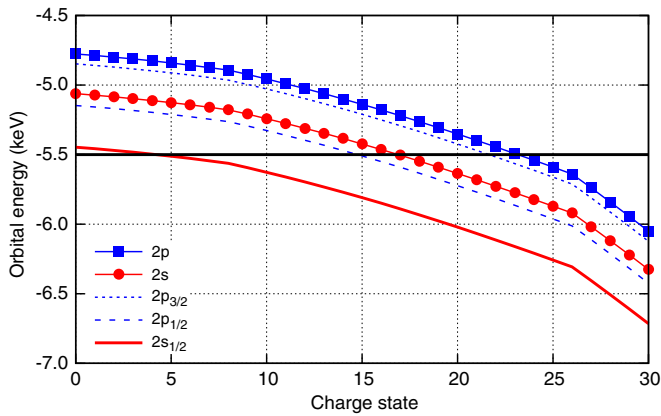
FIG. 2. L-shell orbital energies of the ground configuration of Xe ions with and without relativistic effects.

FIG. 4. Charge-state distributions of Xe at 5.5 keV, after volume integration with a peak fluence of 5.3×10^{10} photons/μm^2.

$2p_{1/2}$, and $2p_{3/2}$) are plotted with lines only. For the whole range of charge states, the $2s_{1/2}$ orbital energies are lower by about 400 eV than the $2s$ orbital energies, and the $2p$ orbital energies are split into the $2p_{1/2}$ and $2p_{3/2}$ by about 300 eV. Therefore, relativistic energy corrections may affect ionization dynamics in the following ways. First, the photoionization cross section of neutral Xe at 5.5 keV becomes higher because the ionization potential of $2s_{1/2}$ is closer to the photon energy. Second, the spin-orbit splitting allows decay channels that are completely absent in the nonrelativistic calculations, for example, the $L_2 - L_3 X$ and $M_2 - M_3 X$ channels in Table III. Both effects may enhance the degree of multiple ionization. Third, the sequence of ionization events in the relativistic case stops earlier than that in the nonrelativistic case. As shown in Fig. 2, $2s$ photoionization at 5.5 keV stops at Xe^{17+} in the nonrelativistic case, whereas $2s_{1/2}$ photoionization stops at Xe^{5+} in the relativistic case. Note that this effect suppresses the yields of higher charge states, unless we consider resonance-driven processes beyond the direct one-photon ionization limit.

We plot the mean charge of Xe at 5.5 keV as a function of fluence for the four different cases (with/without relativistic effects and with/without resonance effect) in Fig. 3. The pulse duration is 30 fs FWHM. The spectral bandwidth of the x-ray pulse is assumed to be 1% (55 eV) for the resonance calculations. All computational parameters used are listed
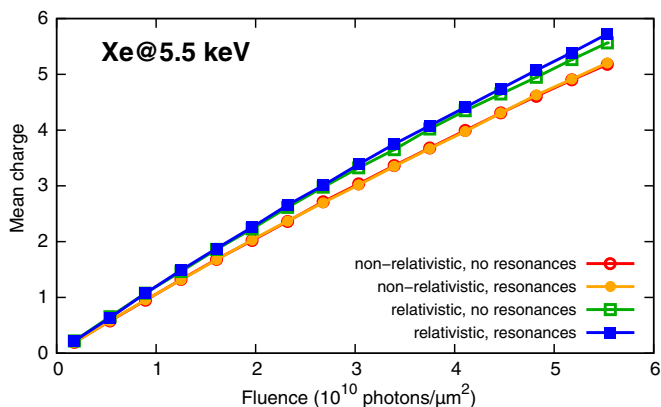

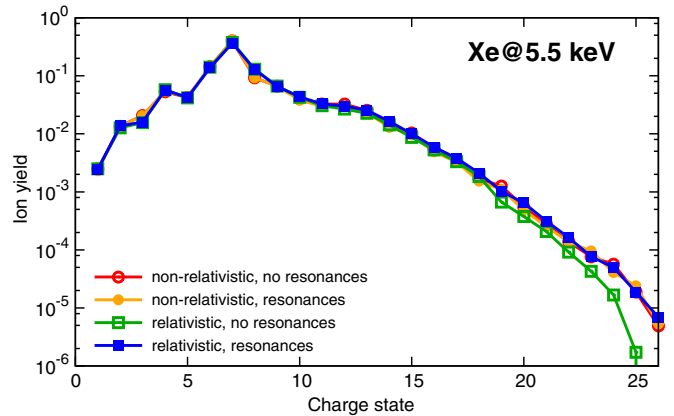FIG. 3. Mean charge of Xe at 5.5 keV as a function of fluence.

in Table IV. One can see that the relativistic calculations (green and blue squares) yield higher mean changes than the nonrelativistic calculations (red and orange circles). The difference in the mean charges is due to the difference in photoionization cross sections of neutral Xe at 5.5 keV: 0.166 Mb in the nonrelativistic case and 0.186 Mb in the relativistic case.

On the other hand, one can see counterintuitive results when the CSDs are examined. Figure 4 shows Xe CSDs at 5.5 keV for the four different cases. A peak fluence of 5.3×10^{10} photons/μm^2 is used for volume integration [11], assuming a Gaussian beam profile. All results are similar to each other, except the relativistic calculation without resonances. Note that the mean charge enhancement of the relativistic case in Fig. 3 is not clearly shown in the CSDs because of the logarithmic scale of the ion yields. It is surprising to see that, without resonances, the relativistic calculation (green, open squares) underestimates the yields of highly charged ions in comparison with the nonrelativistic calculation (red, open circles), which is opposite to the expectation from Refs. [17,24] that those for the relativistic calculation would be enhanced. Since direct one-photon ionization closes at $+5$ in the relativistic case, which is much earlier than $+17$ in the nonrelativistic case, the ion yields in higher charge states are suppressed, even though the mean charge is enhanced.

Next, let us compare the nonrelativistic results without resonances (red, open circles) and with resonances (orange, filled circles) in Fig. 4. It is worthwhile to note that resonance-driven multiple ionization here is resonance-*enhanced* [15] (both photoionization and resonant excitation are allowed), not resonance-*enabled* [16] (which would be the case if only resonant excitation were possible). In the nonrelativistic case, when resonant photoexcitation from $2s$ starts at Xe^{17+}, all $2p$ electrons are still available for photoionization. Since the $2p$ photoionization cross section (0.11 Mb) is much larger than the $2s \rightarrow np$ resonant photoexcitation cross section ($\sim$1 kb), the $2p$ photoionization is the predominant process for ionization. Therefore, resonant excitation only enhances the ionization yields a bit, in addition to photoionization. Even when $2p$ photoionization closes at $+23$, many valence electrons are still available for photoionization, and their cross section is similar to the resonant excitation cross section. Thus one can
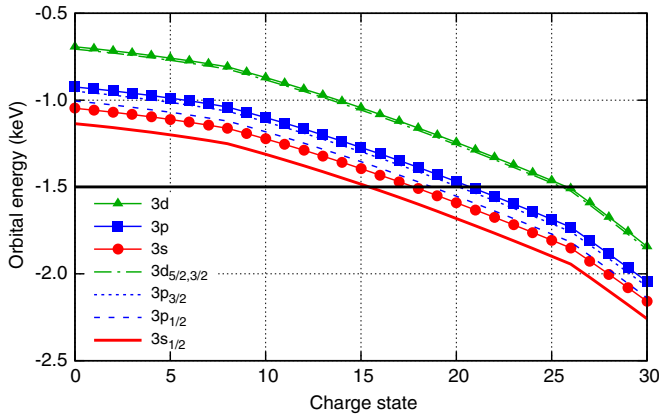
FIG. 5. M-shell orbital energies of the ground configuration of Xe ions with and without relativistic effects.

FIG. 6. Mean charge of Xe at 1.5 keV as a function of fluence.

see from Fig. 4 that the resonance effect at 5.5 keV at the given peak fluence is almost negligible for the nonrelativistic calculations.

The situation is somewhat different when both relativistic and resonance effects are taken into account. Let us compare the relativistic results without resonances (green, open squares) and with resonances (blue, filled squares) in Fig. 4. Since the direct one-photon ionization in the relativistic calculations stops much earlier than that in the nonrelativistic calculations, the enhancement effect due to resonant excitation becomes more visible. One can clearly see that the resonance effect enhances the yields of high charge states in the relativistic case, in contrast to the nonrelativistic case. It turns out that the relativistic, resonant results (blue, filled squares) coincidentally overlap with the nonrelativistic results (red and orange circles).

B. X-ray multiphoton ionization dynamics of Xe at 1.5 keV

At a photon energy of 1.5 keV, M-shell electrons of neutral Xe can be ionized. The M-shell photoionization stops as the charge increases when the M-shell ionization potential of the charge state is higher than the photon energy. After this point, resonant photoexcitation can occur and Xe ions can further ionize via REXMI [15,16]. Figure 5 shows the M-shell orbital energies of the ground configuration of Xe ions as a function of charge state. The nonrelativistic results are plotted with lines and symbols, while the relativistic results are plotted with lines only. The relativistic $3s_{1/2}$ orbital energy is lower than the nonrelativistic $3s$ orbital energy by about 100 eV. The spin-orbit splitting for $3p$ is about 100 eV, but the relativistic effects on $3d$ are less than 20 eV up to Xe^{30+}. For the M-shell orbital energies, there are no dramatic changes due to relativistic effects, in contrast to the L-shell case in the previous subsection.

Figure 6 depicts the mean charge of Xe at 1.5 keV as a function of fluence. The pulse duration is 80 fs FWHM. The x-ray energy bandwidth is 1% (15 eV) for the resonance calculations. All computational parameters used are listed in Table IV. The fluence spans up to 2×10^{11} photons/μm^2, which is higher than the one-photon absorption saturation fluence of neutral Xe at 1.5 keV ($\sim 1.1 \times 10^{10}$ photons/μm^2).
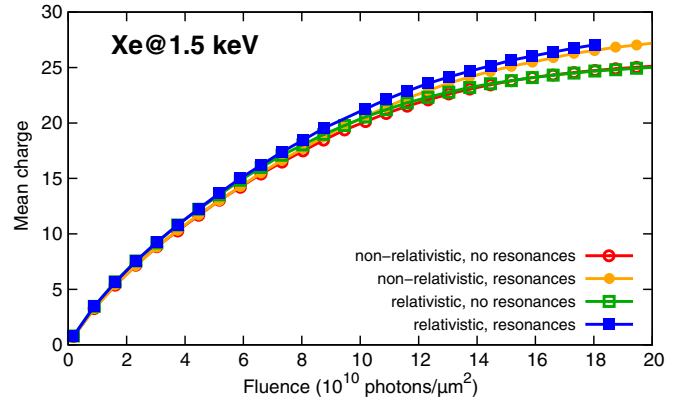
In the low fluence regime, the relativistic calculations (green and blue squares) are a bit higher than the nonrelativistic calculations (red and orange circles). But the mean charges with resonances (orange filled circles and blue filled squares) exceed those without resonances in the high fluence regime, due to REXMI [15,16]. At this photon energy with higher fluences, it is expected that the resonance effect is more pronounced than the relativistic effect.

The calculated CSDs of Xe at 1.5 keV are shown in Fig. 7. A peak fluence of 1.3×10^{11} photons/μm^2 is used for volume integration, assuming a Gaussian beam profile. Let us compare the nonrelativistic cases with and without resonances (red open circles versus orange filled circles). Without resonances, the predicted highest charge state is $+27$, because the direct one-photon ionization from M shell is closed at Xe^{26+}. Note that production of charge states higher by $+1$ or $+2$ is possible via multiple-core-hole states, but their yields are quite low. Including the REXMI mechanism dramatically enhances the yields of high charge states, similar to Ref. [18]. Next, we consider the relativistic effect without resonance (red open circles versus green open squares). As expected, there is no significant change in the relativistic calculation compared to the nonrelativistic calculation (see Fig. 5).

However, our calculation with both relativistic treatment and resonant excitation illustrates that there is an interplay
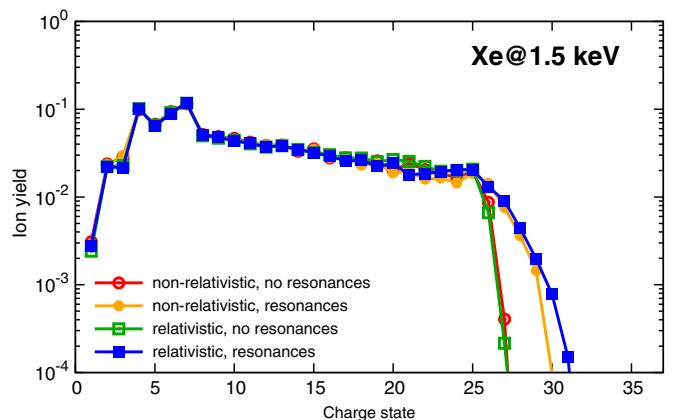

FIG. 7. Charge-state distributions of Xe at 1.5 keV, after volume integration with a peak fluence of 1.3×10^{11} photons/μm^2.
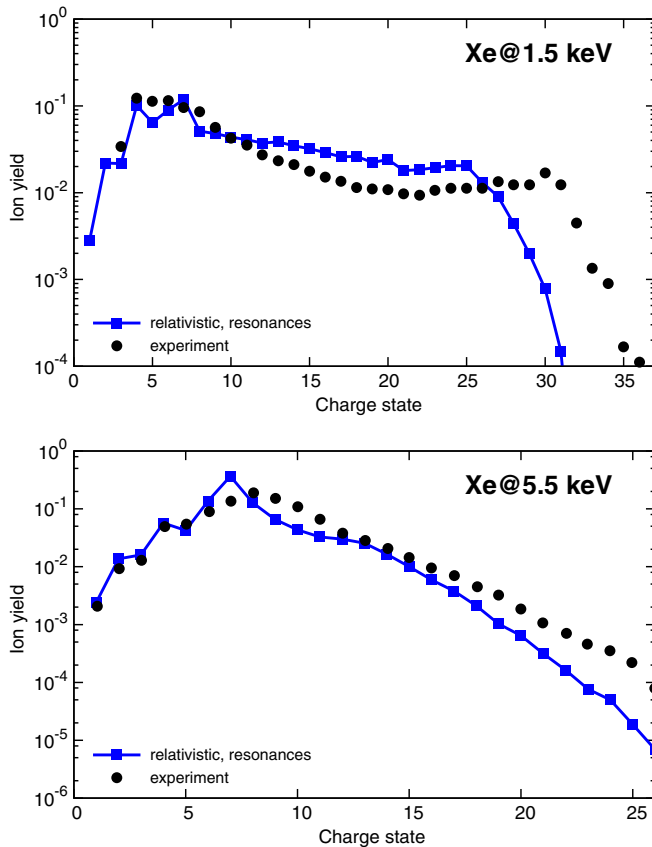
FIG. 8. Charge-state distribution of Xe at 1.5 keV and 5.5 keV compared with experimental data [16,17].

extension is considered to be important because relativistic effects on ion CSDs could become significant in heavy atoms. Our approach is to introduce leading-order relativistic energy corrections via perturbation theory, and cross sections and rates are correspondingly reformulated. We have confirmed that the calculated energy corrections, cross sections, and rates are in good agreement with the literature. Also we have extended XATOM to include resonant photoexcitation processes in both nonrelativistic and relativistic treatments.

We have calculated CSDs of Xe atoms after interacting with intense x-ray pulses at 5.5 keV and 1.5 keV, respectively. At the former photon energy, the ionization dynamics are influenced by relativistic effects, because deep inner-shell electrons are initially ionized. On the other hand, at the latter photon energy, the resonance effect plays a particularly important role in the ionization dynamics at high x-ray intensity. By using the extended XATOM toolkit, we have examined the relativistic effect and the resonance effect separately, and have found a synergy effect when both of them are applied together in our calculations. We have demonstrated that, generally speaking, both effects must be taken into account in x-ray multiphoton ionization dynamics calculations. But do these effects resolve all discrepancies with experiment?

In Fig. 8, we compare the experimental and present theoretical Xe CSDs, at 1.5 keV [16] and 5.5 keV [17], respectively. The theory results shown include both relativistic and resonance effects. For this comparison we have performed the volume integration based on the x-ray beam parameters that were determined in each experiment. Our theoretical prediction still underestimates the yields of highly charged ions in the CSD at both photon energies. This might be due to our mean-field approach and a lack of higher-order many-body processes such as shakeoff processes and/or double Auger decays in our theoretical approach. The discrepancy between theory and experiment might also be attributed to uncertainties in the x-ray beam parameters, such as the spatial beam profile and spectral bandwidth. Therefore, for a more quantitative understanding of x-ray multiphoton ionization dynamics, it is desirable to improve the theoretical treatment for x-ray-induced processes and the calibration of the x-ray beam parameters in experiment.

between the two effects. The relativistic calculation with resonances (blue filled squares) clearly shows higher populations than the nonrelativistic calculation with resonances (orange filled circles) for highly charged ions beyond the direct one-photon ionization limit (+26). In the relativistic case, the REXMI mechanism starts earlier and the spin-orbit splittings increase chances to hit resonances. Therefore, relativistic effects can further enhance the REXMI effect, producing more high charge states.

IV. CONCLUSION AND PERSPECTIVE

In this paper, we have extended the XATOM toolkit to a relativistic version in order to further study x-ray multiphoton ionization dynamics of Xe atoms in XFEL beams. This

ACKNOWLEDGMENTS

[1] T. A. Carlson, W. E. Hunt, and M. O. Krause, Phys. Rev. **151**, 41 (1966).

[2] T. Mukoyama, J. Phys. Soc. Jpn. **55**, 3054 (1986).

[3] T. Mukoyama, T. Tonuma, A. Yagishita *et al.*, J. Phys. B **20**, 4453 (1987).

[4] A. G. Kochur, A. I. Dudenko, V. L. Sukhorukov, and I. D. Petrov, J. Phys. B **27**, 1709 (1994).

[5] A. M. El-Shemi and Y. A. Lofty, Eur. Phys. J. D **32**, 277 (2005).

[6] C. Pellegrini, A. Marinelli, and S. Reiche, Rev. Mod. Phys. **88**, 015006 (2016).

[7] C. Bostedt, S. Boutet, D. M. Fritz *et al.*, Rev. Mod. Phys. **88**, 015007 (2016).

[8] M. Yabashi, H. Tanaka, T. Tanaka *et al.*, J. Phys. B **46**, 164001 (2013).

[9] J. Feldhaus, M. Krikunova, M. Meyer *et al.*, J. Phys. B **46**, 164002 (2013).

[10] R. Santra and L. Young, in *Synchrotron Light Sources and Free-Electron Lasers*, edited by E. J. Jaeschke *et al.* (Springer, Switzerland, 2016), pp. 1233–1260.

[11] L. Young, E. P. Kanter, B. Krässig *et al.*, Nature (London) **466**, 56 (2010).

[12] N. Rohringer and R. Santra, Phys. Rev. A **76**, 033416 (2007).

[13] G. Doumy, C. Roedig, S.-K. Son *et al.*, Phys. Rev. Lett. **106**, 083002 (2011).

[14] K. Motomura, H. Fukuzawa, S.-K. Son *et al.*, J. Phys. B **46**, 164024 (2013).

[15] B. Rudek, D. Rolles, S.-K. Son *et al.*, Phys. Rev. A **87**, 023413 (2013).

[16] B. Rudek, S.-K. Son, D. Rolles *et al.*, Nat. Photon. **6**, 858 (2012).

[17] H. Fukuzawa, S.-K. Son, K. Motoyama *et al.*, Phys. Rev. Lett. **110**, 173005 (2013).

[18] P. J. Ho, C. Bostedt, S. Schorb, and L. Young, Phys. Rev. Lett. **113**, 253001 (2014).

[19] P. J. Ho, E. P. Kanter, and L. Young, Phys. Rev. A **92**, 063430 (2015).

[20] W. Xiang, C. Gao, Y. Fu, J. Zeng, and J. Yuan, Phys. Rev. A **86**, 061401 (2012).

[21] S.-K. Son, K. Toyota, O. Geffert, J. M. Slowik, and R. Santra, XATOM—an integrated toolkit for x-ray and atomic physics, CFEL, DESY, Hamburg, Germany, 2016, Rev. 2508.

[22] S.-K. Son, L. Young, and R. Santra, Phys. Rev. A **83**, 033402 (2011).

[23] Z. Jurek, S.-K. Son, B. Ziaja, and R. Santra, J. Appl. Crystallogr. **49**, 1048 (2016).

[24] S.-K. Son and R. Santra, Phys. Rev. A **85**, 063415 (2012).

[25] R. Santra, J. Phys. B **42**, 023001 (2009).

[26] D. A. Varshalovich, A. N. Moskalev, and V. K. Khersonskii, *Quantum Theory of Angular Momentum* (World Scientific, Singapore, 1988).

[27] J. Slater, Phys. Rev. **81**, 385 (1951).

[28] R. Latter, Phys. Rev. **99**, 510 (1955).

[29] D. A. Telnov and Shih-I Chu, Phys. Rev. A **59**, 2864 (1999).

[30] F. Herman and S. Skillman, *Atomic Structure Calculations* (Prentice-Hall, Englewood Cliffs, NJ, 1963).

[31] J. D. Bjorken and S. D. Drell, *Relativistic Quantum Mechanics* (McGraw-Hill, New York, 1964).

[32] L. L. Foldy and S. A. Wouthuysen, Phys. Rev. **78**, 29 (1950).

[33] C. C. Lu, T. A. Carlson, F. B. Malik *et al.*, At. Data **3**, 1 (1971).

[34] K.-N. Huang, M. Aoyagi, M. S. Chen, B. Crasemann, and H. Mark, At. Data **18**, 243 (1976).

[35] A. C. Thompson *et al.*, X-Ray Data Booklet (Center for X-Ray Optics and Advanced Light Source, Lawrence Berkeley National Laboratory, Berkeley, CA, 2009), http://xdb.lbl.gov.

[36] J. W. Cooper, Phys. Rev. **128**, 681 (1962).

[37] S. T. Manson and J. W. Cooper, Phys. Rev. **165**, 126 (1968).

[38] J. H. Scofield, Lawrence Livermore National Laboratory Report No. UCRL-51326, 1973 (unpublished).

[39] W. N. Asaad, Nucl. Phys. **44**, 415 (1963).

[40] J. M. Sampaio, T. I. Madeira, M. Guerra, F. Parente, J. P. Santos, P. Indelicato, and J. P. Marques, Phys. Rev. A **91**, 052507 (2015).